Hall Effect Sensors using Polarized Electron Cloud Spin Orientation Control

Journal:	*Microscopy Research and Technique*
Manuscript ID	MRT-20-304
Wiley - Manuscript type:	Research Article
Date Submitted by the Author:	04-Jul-2020
Complete List of Authors:	Arumona, A.E.; Ton Duc Thang University Garhwal, A; Amity University Rajasthan Youplao, P.; Rajamangala University of Technology Isan, Electrical Engineering Amiri, IS; Ton Duc Thang University Ray, K; Amity University Jaipur Punthawanunt, S; Kasetsart University Yupapin, Preecha
Classifications:	computational optical sectioning microscopy < LIGHT MICROSCOPY
Keywords:	Hall effect sensors, Voltage sensor, Current sensor, Temperature sensor

Hall Effect Sensors using Polarized Electron Cloud Spin Orientation Control

A.E. Arumona[1,2,3,a], A. Garhwal[4], P. Youplao[5], I.S. Amiri[1], K. Ray[6], S. Punthawanunt[7], P. Yupapin[1,2*]

[1]Computational Optics Research Group, Advanced Institute of Materials Science, Ton Duc Thang University, District 7, Ho Chi Minh City, Vietnam; [2]Faculty of Applied Sciences, Ton Duc Thang University, District 7, Ho Chi Minh City, Vietnam; [3]Division of Computational Physics, Institute for Computational Science, Ton Duc Thang University, Ho Chi Minh City 700000, Vietnam; [4]Amity School of Applied Sciences, Amity University Rajasthan, Jaipur, 302002, India; [5]Department of Electrical Engineering, Faculty of Industry and Technology, Rajamangala University of Technology Isan Sakon Nakhon Campus, Sakon Nakhon 47160, Thailand; [6]Amity School of Applied Sciences, Amity University Rajasthan, Jaipur, 302002, India; [7]Faculty of Science and Technology, Kasem Bundit University, Bangkok 10250, Thailand; [a]arumonaarumonaedward.st@tdtu.edu.vn; *Corresponding author: e-mail:preecha.yupapin@tdtu.edu.vn;

Abstract: A silicon microring circuit embedded gold film with unique characteristics is proposed for Hall effect, current, and temperature sensing applications. The microring circuit is operated by the input polarized laser sources, in which the space-time distortion control can be employed. A gold film is embedded at the microring center. The whispering gallery mode (WGM) is generated and applied for plasmonic waves, from which the trapped electron cloud oscillation is formed. Through the input port, the input polarized light of 1.55μm wavelength fed into the space-time control circuit. Spin-up $|\uparrow\rangle$ $(|0\rangle)$ and spin-down $|\downarrow\rangle$ $(|1\rangle)$ of polarized electrons results when the gold film is illuminated by the WGM. The electric current passing through the gold film generates a magnetic field (B), which is orthogonal to the electric field. Hall voltage is obtained at the output of the circuit, from which the microring space-time circuit can operate for Hall's effect, current, and temperature sensing device. The simulation results obtained have shown when the input power of 100mW-500mW is applied, the optimum Hall effect, current and temperature sensitivities are 0.12μVT^{-1}, 0.9μVA^{-1} and 6.0 x10^{-2}μVK^{-1}, respectively. The Hall effects, current, and temperature sensors have an optimum response time of 1.9fs.

Research Highlight

[1]-Hall effect sensors using polarized electron cloud spin is novel.
[2]-This is a compact device with realistic parameters that can be fabricated and implemented.
[3]-The proposed circuit can be applied for voltage, current and temperature sensors.
[4]-By using the electron cloud spin, the related microspic sensors can be applied.
[5] The wireless (remote) sensor is also possible.

Keywords: Hall effect sensors; Voltage sensor; Current sensor; Temperature sensor; Plasmonic sensors

1. Introduction

The Hall effect is the effect that results from the electric field that is orthogonal to the magnetic field in a thin film or any metallic material where the electrical current passes through generating an electric field. The Hall voltage (V_H) results from the Hall effect generated by electrical current in a conductor, where the magnetic field is formed and orthogonal to the electrical current. The most popular use of the Hall effect is in sensing (Alpert et al., 2019; Ramsden, 2006; Anuchin et al., 2019). Sun et al. (Sun et al., 2016) have designed a wireless electrical current sensor, which consists of a wireless module, Hall sensor, and energy harvester. The wireless Hall current sensor is applied for sensing and energy harvesting. The generated power is 4.3 μW when 1A zip-cord is applied with a load resistor of 217Ω. From which a 4A zip-cord is applied with a power of 68.80 μW, which is suitable for Hall wireless current sensors. The sensitivity of the work is 0.85 mVA^{-1}, with current ranging from 1A to 130A. The size of the wireless Hall current sensor is in millimeters (mm). Weiss et al. (Weiss et al., 2019) designed a coreless current sensor that is employed for Hall-effect sensing. The current sensor is based on a closed-loop principle, from which the close loop current sensor tends to have large bandwidth, and higher accuracy when compared to the current sensor based only on magnetic field circular arrays. The close and open-loop operations are employed for sensing. Both close and open-loop operations use the fluxgate and Hall effect sensors. The experimental results have shown that the Hall sensors can reduce the sensitivity drift more than the fluxgate sensor. The accuracies of 0.2% and 0.4 % are achieved for fluxgate and Hall sensors, respectively. The Hall sensor in open-loop and closed-loop operations have a sensitivity of 2.67 mVA^{-1} and 0.5 mVA^{-1}, respectively. The fluxgate sensors in open-loop and closed-loop operations have a sensitivity of 3.35 mVA^{-1} and 0.50 mVA^{-1}, respectively. The size of the coreless current is in millimeters (mm). Itzke et al. (Itzke et al., 2019) studied the importance of conductor position in Hall effect electrical current sensor. The Hall effect sensor is based on the magnetic field of circular arrays, which have been theoretically and experimentally studied. The experimental study involves 6 Hall effect sensors that are uniformly arranged. The study involves the calculation of the current for all 6 Hall-effect sensors employed in the experiment. The Kelvin-Stokes theorem is employed in the calculation of the current. The size of the circular Hall effect sensor is in millimeters (mm). The sensitivity measurements have been taken several times with the average

sensitivity value of -1.71 mVA^{-1}. Dewi et al. (Dewi et al., 2016) developed a new DC current sensor, where the sensitivity measurements have been taken several times with the average sensitivity value. The DC sensor is designed and employed for Hall-effect sensing. The size of the current sensor is in millimeters (mm), where the sensitivity of 1.2 mVG^{-1} is achieved. Kachniarz et al. (Kachniarz et al., 2019) developed a new Hall-effect sensing device. The device has a sensing material that is graphene. The sensor is employed for sensing the magnitude of the magnetic field. The size of the new hall effect sensor is in millimeters (mm). The sensitivity of 50 V $(AT)^{-1}$ is achieved. White et al. (White et al., 2018) designed a large micro device that is based on the principle of Hall effect. The device can measure both the temperature and the current from the line current. The temperature range of -183^{0}C to 252^{0}C is employed for the study. The sensitivity of the Hall effect sensor is in the range of 80$VA^{-1}T^{-1}$ to 113$VA^{-1}T^{-1}$. The sensitivity of 113$VA^{-1}T^{-1}$ is obtained at 25^{0}C, while the sensitivity of 80$VA^{-1}T^{-1}$ is obtained at 252^{0}C. Ciuk et al. (Ciuk et al., 2019) designed a Hall sensor device. The device consists of graphene grown on a 4H-silicon carbide substrate. The device serves as a temperature Hall sensor. The temperature range of 300K to 770K is employed for the investigation. The sensitivity of 80$VA^{-1}T^{-1}$ is obtained. Oszwaldowski and Berus (Oszwaldowski and Berus, 2007) designed a temperature Hall sensor, which is an experimental study. The device consists of indium antimonide grown on gallium arsenide. The temperature range of 200K to 800K is employed for the study. The sensor sensitivity of 0.1$VA^{-1}T^{-1}$ is obtained. Recently, we have found that the use of microring embedded metallic films have shown the interesting results for various applications, especially, for electro-optic behaviors are involved (Ali et al., 2018; Arumona et al., 2020a; 2020b; Pornsuwancharoen et al., 2017; Ponsuwancharoen et al., 2019). In this present work, the space-time microring circuit is employed for Hall effects, temperature, and current sensing. The microring circuit is a space-time control circuit, which has three advantages in this work. Firstly, its side is small. The area of the microring system is $12 \times 20\ \mu m^2$, which is very small compared to other Hall effects and current sensing devices. Secondly, the microring system has a dual mode of operation. That is, it can operate via a wireless(remote) connection or by cable connection. Finally, the microring system can be employed for Hall effect and Hall effect current sensing. The simulation programs involved in this work are the Optiwave FDTD and Matlab programs. The Optiwave FDTD is first used to simulate the structure, where the whispering gallery mode (WGM) is observed at the microring center (Pornsuwancharoen et al., 2017; Punthawanunt et al., 2018), and from the simulation results, parameters are extracted. The Matlab program employs the extracted parameters to simulate the Hall effect, temperature, and current sensing.

2. Theoretical Background

The fabrication structure and the sensing diagram of the microring circuit are shown in Figure 1. The Hall sense probe is formed by passing the electric current through the gold film embedded at the center microring, which is given by an equation (1)(Preston and Dietz, 1991).

$$\boldsymbol{Ein = BV_d} \quad \textbf{1}$$

where E_{in} is the input polarized source via the input port of the system which is given in equation (2), B is defined as strength of magnetic field, and V_d is defined as the drift velocity of the electrons which is given by the following equation.

The input polarized light (optical field) is given as (Arumona et al., 2020c):

$$\boldsymbol{E_{in} = E_o.\exp(-ik_z z)} \quad \textbf{2}$$

$k_z = \frac{2\pi}{\lambda}$, is the wave number, and the field's amplitude is defined by E_0, the distance of propagation is defined by z, and the input optical field wavelength is defined by λ. The drift velocity is given as (Preston and Dietz, 1991):

$$\boldsymbol{V_d = \frac{I}{nqA}} \quad \textbf{3}$$

where the electron density is defined by n, the electron charge is defined by q, the electric current is defined by I, and the area of the gold film is defined by A.

The space-time function control is given as:

$$\boldsymbol{E_{add} = F\, e^{\pm i\omega t}} \quad \textbf{4}$$

where the amplitude is defined by F, ω is defined as the angular velocity, and time is defined by t. The $\pm$ sign shows the axis in both side of time, which is applied for spin projection direction. The refractive index induced by the nonlinear Kerr effect is given as $N = \boldsymbol{n_0 + n_2 P / A_{eff}}$, where $n_0$is defined as linear refractive index,n_2 is defined as the nonlinear refractive index. The optical power is defined by P, the waveguide's effective core area is defined by A_{eff}.

The Drude model (Werner, 2017; Tunsiri et al., 2019), which describes the electron behavior and coupling of light in the gold film is given as:

$$\boldsymbol{\epsilon(\omega) = 1 - \frac{nq^2}{\epsilon_0 m\omega^2}} \quad \textbf{5}$$

Where the relative permittivity is defined by ϵ_0. The electron mass is defined by m. The plasma frequency results from the angular frequency at resonance and is given as:

$$\boldsymbol{\omega_p = \left[\frac{nq^2}{\epsilon_0 m}\right]^{-1/2}} \quad \textbf{6}$$

Where $n = \frac{\omega_p^2}{q^2}\epsilon_0 m$ is the electron density derived from an equation (5).

Hall effect potential difference (Hall voltage, V_H) is given as (Preston and Dietz, 1991):

$$V_H = \frac{IB}{nqd} \quad (7)$$

where d is the thickness of the gold film embedded at the center microring. The Hall coefficient (R_H) is given as (Mirmira, and Fletcher, 1998):

$$R_H = \frac{V_H\, d}{IB} \quad (8)$$

Hall mobility is given as (Mirmira, and Fletcher, 1998):

$$\mu_n = \sigma n R_H \quad (9)$$

where σ is the conductivity.

The equations describing the output fields of the system (Phatharacorn et al., 2016) are given as:

$$E_{th} = m_2 E_{in} + m_3 E_{add} \quad (10)$$

$$E_d = m_5 E_{add} + m_6 E_{in} \quad (11)$$

where m_2,m_3,m_5, m_6 are well explained Phatharacorn et al. (Phatharacorn et al., 2016).

The system output are normalized intensities given as:

$$\frac{I_{th}}{I_{in}} = \left[\frac{E_{th}}{E_{in}}\right]^2 \quad (12)$$

$$\frac{I_d}{I_{in}} = \left[\frac{E_d}{E_{in}}\right]^2 \quad (13)$$

The change in temperature(ΔT) is given as (Preston and Dietz, 1991):

$$\Delta T = \frac{P_{in} d}{K_{Au} A} \quad (14)$$

where P_{in} is defined as the input light power, K_{Au} is defined as the thermal conductivity of gold film.

From Figure 1, the z-axis is a propagation axis, while the space-time control axes are x- and y-axes. Hence, the magnetic field components perpendicular to the electric field are projected to x- and y-axes to obtain the Hall effects results at the drop port. The optical feedback is protected by an optical isolator. The throughput port output can be connected to the transmission network for long-distance links. The space-time distortion control is input via Add port, from which the electron cloud spins are formed and calculated by the Matlab program.

3. Results and Discussion

The microcircuit system consists of two linear waveguides, a microring center with two phase modulators at its sides, and a gold film embedded at the center microring. The space-time control circuit is proposed for electron cloud spin orientation and projection (Arumona et al., 2020d; Buruangses et al., 2020). The fabrication structure and sensing diagram is as shown in Figure 1. The system has two outputs namely the throughput port labelled Eth, and drop port labelled Ed. The input port is labelled Ein while the add port is usually for modulation or multiplexing is labelled Eadd. The Optiwave FDTD program version 12.0 (OptiFDTD, 2020) is used as a first step to simulate the structure. The mesh cell size of 399, 71, 456 in the x, y, and z axes are employed with the automatic implementation of the grid size by the Optiwave program. The simulation is run for 20,000-time steps to obtain resonant results and parameters extracted, which are employed by the Matlab program. Matlab program simulates the Hall effect and Hall effect current sensing. The surrounded environmental changes on the sensing circuit and affect the Hall sensor sensitivity, from which the related measurement can be obtained. As given in equation (2) the input light of 1.55μm wavelength through the input port enters the system as given in equations (10) and (11). The electric current passing through the gold film generates a magnetic field (B) that is orthogonal to E (electric field) as given in equation (1). As given in equation (4) the signal at the add port is the space-time function where the gold film becomes the Hall effect sensing probe and at the space-time control circuit output the Hall voltage (V_H) is produced. The spin up $|\uparrow\rangle$ $(|0\rangle)$ and spin down $|\downarrow\rangle$ $(|1\rangle)$ of electrons results when the gold film is illuminated by light where the electron density[$n = \frac{\omega_p^2}{e^2}\epsilon_0 m$]is formed by the electron cloud oscillations. The electrons are trapped inside the microring and via cable connection can be transported. Figure 2 shows the Optiwave graphical results where the WGM is observed at the microring center with suitable parameters given in Table 1. The WGM phenomenon is made possible because of the nonlinearity effect induced by the two-phase modulators at the sides of the microring center.

The plot of the normalized output (as given in equations (12) and (13)) is shown in Figure 3. the input light power is varied from 100-500mW. The polarized electron spin-up (blue) spin-down (red) are shown at the throughput and drop ports in Figure 3 (a)-(e), respectively. The plot of the Hall effect sensor is shown in Figure 4. The input power is varied from 100-500mW. The Hall voltage is directly proportional to the magnetic field strength (B). From Figure 4 with the input power of 100mW, the electric current passing through the gold film generates a high magnetic field strength (B) and with the input power of 200mW-500mW respectively, the magnetic field strength decreases. That is, the increase in the input light power leads to a decrease in the magnetic field strength generated by the embedded gold film in the space-time control circuit. The sensitivity of the Hall effect with the

input power of 100mW-500mW as shown in Figure 4 are $0.05\mu VT^{-1}$, $0.08\mu VT^{-1}$, $0.10\mu VT^{-1}$, $0.11\mu VT^{-1}$, and $0.12\mu VT^{-1}$ respectively. The sensitivity increases as the input power increases and decreases as the input power decreases. That is, the lower the sensitivity the greater the magnetic field strength value while the higher the sensitivity value the lower the magnitude of the magnetic field strength. The plot of the Hall mobility and the electron density is shown in Figure 5. Hall mobility is the movement of electrons as a result of the Hall effect, which is directly proportional to the electron density. Input power is varied from 100mW to 500mW as shown in Figure 5, the output is constant for all the input light power. The plot of the Hall effect current sensor is shown in Figure 6. The input power is varied from 100mW to 500mW. The Hall voltage is directly proportional to the electric current. From Figure 6 with the input power of 100mW, the electric current value is small and with the input power in the range 200mW-500mW, the value of the electric current increases. That is, the increase in the input light power leads to an increase in the value of the electric current in the space-time control circuit.

The sensitivity of the Hall effect current sensor with the input power of 100mW-500mW as shown in Figure 6 are $0.9\mu VA^{-1}$, $0.6\mu VA^{-1}$, $0.5\mu VA^{-1}$, $0.42\mu VA^{-1}$, and $0.38\mu VA^{-1}$ respectively. The sensitivity decreases as the input power increases and increases as the input power decreases. That is, the higher the sensitivity the lower the electric current value while the lower the sensitivity value the higher the electric current value. The plot of the response time is shown in Figure 7 (a)-(b). The Hall effect current sensor response time is plotted in Figure 7 (a) while the Hall effect sensor response time is plotted in Figure 7 (b). The input power is varied from 100mW to 500mW. The Hall effect current sensitivity with the input power in the range 100mW-500mW is shown in Figure 7(a), where the optimum response time of 1.9fs is obtained. The Hall effect sensitivity with the input power of 100mW-500mW is shown in Figure 7(b), where the optimum response time of 1.9fs is obtained. Figure 8(a) is the plot of the ΔT and Hall voltage which forms the temperature Hall sensor with the input power of 100mW-500mW. The temperature Hall sensitivity of $0.03\mu VK^{-1}$, $0.015\mu VK^{-1}$, $0.011\mu VK^{-1}$, $0.008\mu VK^{-1}$, and $0.006\mu VK^{-1}$ are obtained respectively for the input power varying from 100mW to 500mW. point, which is the stopping situation. Figure 8(b) is the plot of ΔT and the Hall current sensitivity with the input power varying from 100mW to 500mW. The sensitivities of $0.9\mu VA^{-1}$, $0.6\mu VA^{-1}$, $0.5\mu VA^{-1}$, $0.42\mu VA^{-1}$, and $0.38\mu VA^{-1}$ are obtained at 100K, 200K, 300K, 400K, and 500K, respectively. Figure 8(c) is the plot of ΔT and the Hall effect sensitivity with the input power of 100mW-500mW. The sensitivities of $0.05\mu VT^{-1}$, $0.08\mu VT^{-1}$, $0.10\mu VT^{-1}$, $0.11\mu VT^{-1}$, and $0.12\mu VT^{-1}$ are obtained at 100K, 200K, 300K, 400K, and 500K, respectively. Figure 8(d) is the plot of the response time of the temperature Hall sensitivities, where the optimum response time of 1.9fs is obtained.

4. Conclusion

A microring system is proposed for Hall effect current sensor, Hall effect sensor, and temperature Hall sensor. The system consists of a gold film embedded at the center microring. The excitation of the gold film by the input light (electric field) leads to electron cloud oscillation where the spin up and spin down of electrons results from the electron density formed. The electric current passing through the gold film generates a magnetic field that is orthogonal to the electric field and at the output of the microring system the Hall voltage is produced. The input power is varied from 100mW to 500mW and the Hall effect sensitivities of $0.05\mu VT^{-1}$, $0.08\mu VT^{-1}$, $0.10\mu VT^{-1}$, $0.11\mu VT^{-1}$, $0.12\mu VT^{-1}$ are obtained. The Hall effect current sensitivities of $0.9\mu VA^{-1}$, $0.6\mu VA^{-1}$, $0.5\mu VA^{-1}$, $0.42\mu VA^{-1}$, $0.38\mu VA^{-1}$ are obtained. The temperature Hall sensitivities of $0.03\mu VK^{-1}$, $0.015\mu VK^{-1}$, $0.011\mu VK^{-1}$, $0.008\mu VK^{-1}$, and $0.006\mu VK^{-1}$are obtained. The optimum Hall effect, Hall effect current, and temperature Hall sensors response time of 1.9fs are obtained. The results obtained show that the silicon microring circuit embedded gold film can be employed as a sensing circuit in microsystems for Hall effect related sensing applications. The use of the integrated Hall sensors can also be available for remote and network sensors in both wireless and cable connections.

Acknowledgment

The authors would like to acknowledge the research funding support from the Foundation of Science and Technology Development of Ton Duc Thang University (FOSTECT), website: http://fostect.tdt.edu.vn, under the research grant number FOSTECT.2017BR.07.

Conflict of Interest

The authors have declared that this work has no conflict of interest.

References

Ali, J., Youplao, P., Pornsuwancharoen, N., Jalil, M.A., Chiangga, S., Amiri, I.S., Punthawanunt, S., Aziz, M.S., Singh, G., Yupapin, P., Grattan, K.T.V.(2018). Nano-capacitor-like model using light trapping in plasmonic island embedded microring system. Results in Physics, 10, 727-730.

Alpert, H.S., Dowling, K.M., Chapin, C.A., Yalamarthy, A.S., Benbrook, S.R., Kock, H., Ausserlechner, U, Senesky, D.G. (2019). Effect of geometry on sensitivity and offset of AlGaN/GaN and InAlN/GaN Hall-effect sensors. IEEE Sensors Journal, 19(10), 3640-3646.

Anuchin, A., Zharkov, A., Shpak, D., Aliamkin, A., Vagapov, Y.(2019). Current derivative measurement using closed-loop Hall-effect current sensor. Journal of Engineering, 2019(17), 4027-4030.

Arumona, A.E. Amiri, I.S., Yupapin, P.(2020a). Plasmonic micro-antenna characteristics using gold grating embedded panda-ring circuit. Plasmonics, 15, 279-285.

Arumona, A.E., Amiri, I.S., Punthawanunt, S., Ray, K., Singh, G, Hharti, G.K., Yupapin, P.(2020b), 3D-quantum interferometer using silicon microring embedded gold grating circuit, Microscopy Research and Techniques, Early view online: https://doi.org/10.1002/jemt.23513

Arumona, A.E., Amiri,I.S., Punthawanunt, S., Ray, K., Yupapin, P.(2020c). Electron density transport using microring circuit for dual-mode power transmission. Optical and Quantum Electronics, 52, 213.

Arumona, A.E., Garhwal, A., Youplao, P., Amiri, I.S., Ray, R., Punthawanunt, S., Yupapin, P.(2020d) "Electron cloud spectroscopy using microring Fabry-Perot sensor embedded gold grating. IEEE Sensors Journal, Early Access, pp. 1-1.

Bunruangses, M., Youplao, P., Amiri, I.S., Pornsuwancharoen, N., Punthawanunt, S., Singh, G., and P. Yupapin, P.(2020). Microring distributed sensors using space-time function control. IEEE Sensors Journal, 20(2) 799-805.

Ciuk, T., Stanczyk, B., Przyborowska, K., Czolak, D., Dobrowolski,A., Jagiello, J., Kaszub, W., Kozubal, M., Kozlowski, R., Kaminski, P.(2019). High-temperature Hall effect sensor based on epitaxial graphene on high-purity semiinsulating 4H-SiC. IEEE Transactions on Electron Devices, 66(7), 3134-3138.

Dewi, S.D.T., Panatarani, C., Joni, I.M.(2016) Design and development of dc high current sensor using Hall-effect method. AIP Conf. Proc., 1712, 030006.

Itzke, A., Weiss, R., Weigel, R.(2019). Influence of the conductor position on a circular array of Hall sensors for current measurement. IEEE Transactions on Industrial Electronics, 66(1), 580-585.

Kachniarz, M., Petruk, O., Strupinski, W., Ciuk, T., Bienkowski, A., Szewczvk, R., Salach, J.(2019). Quasi-free-standing bilayer graphene Hall-effect sensor. IEEE Transactions on Magnetics, 55(1), 4000204.

Langer, G., Hartmann, J., Reichling, M.(1997)Thermal conductivity of thin metallic films measured by photothermal profile analysis. Review of Scientific Instruments, 63(8), 1510-1513.

Mirmira, S.R., Fletcher, L.S.(1998). Review of the thermal conductivity of thin films," Journal of Thermophysics and Heat Transfer, Vol. 12, No. 2, pp. 121-131, 1998.

OptiFDTD Technical Background and Tutorials (Finite Difference Time Domain) Photonics Simulation Software, Version 12.0. http://www.optiwave.com, Searched on 20thMay, 2020.

Oszwaldowski, M. and Berus, T.(2007). High temperature Hall sensors. Sensors and Actuators A, 136, 234-237.

Phatharacorn, P., Chiangga, S., Yupapin, P. (2016). Analytical and simulation of a triple micro whispering gallery mode probe system for a 3D blood flow rate sensor. Applied Optics, 55, 9504-9513.

Pornsuwancharoen, N., Amiri, I.S., Suhailin, F.H., Aziz, M.S., Ali, J., Singh, G., Yupapin, P.(2017). Micro-current source generated by a WGM of light within a stacked silicon-graphene-Au waveguide. IEEE Photon. Technol. Lett., 29(21), 1768 – 1771.

Pornsuwancharoen, N., Youplao, P., Amiri, I.S., Aziz, M.S., Tran, Q.L., Ali, J, Yupapin, P, Grattan, K.T.V.(2019). Multifunction interferometry using the electron mobility visibility and mean free path relationship. Microscopy Research and Techniques, 81(8), 872-877.

Prabhu, A.M., Tsay, A., Han, Z., and V. Van, V.(2010). Extreme miniaturization of silicon add-drop microring filters for VLSI photonics applications, IEEE Photonics Journal, 2(3), 436-444.

Preston, D. W., Dietz, E.R.(1991). The Art of Experimental Physics, John Wiley & Sons, New York, 303–315.

Punthawanunt, S., Aziz, M.S., Phatharacorn, P., Chiangga, S., Ali, J., Yupapin, P.(2018). LiFi cross-connection node model using whispering gallery mode of light in a microring resonator. Microsyst. Technol., 24, 4833-4838.

Ramsden, E.(2006). Hall Effect Sensors—Theory and Applications," 2nd ed.; Elsevier: Amsterdam, Netherlands.

Sun, C., Wen, Y., Li, P., Ye, W., Yang, J., Qiu, J., Wen, J.(2016). Self-contained wireless Hall current sensor applied for two-wire zip-cords. IEEE Transactions on Magnetics, 52(7), 8600204.

Tunsiri, S., Thammawongsa, N., Threepak, T., Mitatha, S., Yupapin, P.(2019). Microring switching control using plasmonic ring resonator circuits for super-channel use. Plasmonics,14, 1669–1677.

Weiss, R., Itzke, A., Reitenspiess, J., Hoffmann, I., Weigel, R.(2019). A novel closed loop current sensor based on a circular array of magnetic field sensors. IEEE Sensors Journal, 19(7), 2517-2524.

Werner, F.(2017). Hall measurements on low mobility thin films. Journal of Applied Physics, 122, 135306.

White, T.P., Shetty, S., Ware, M.E., Mantooth, H.A., Salamo, G.J.(2018) AlGaN/GaN micro-Hall effect devices for simultaneous current and temperature measurements from line currents. IEEE Sensors Journal, 18(7), 2944-2951.

Figure Captions and Table

Figure 1: Hall effects sensor system, where (a) a microring circuit with the embedded gold thin film at the centre ring, where $\boldsymbol{R_L}$, $\boldsymbol{R_R}$, $\boldsymbol{R_S}$: the radii of the left, right, and centre rings, respectively. The coupling coefficients: κ_s = 0.5. $\boldsymbol{r_{Au}}$ is the radius of the gold plate. $\boldsymbol{E_{in}}$, $\boldsymbol{E_{th}}$, $\boldsymbol{E_d}$, and $\boldsymbol{E_{add}}$, represent the electrical fields each at the input, throughput, drop and add ports, respectively, (b) Hall effect sensing diagram.

Figure 2: Optiwave graphical results, where (a) the WGM formed at the microring center, (b) the electric field distribution across the circuit using the selected parameters in Table 1.

Figure 3: Plot of the output of the system in Figure 1 with the different input power, where (a) 100mW, (b) 200mW, (c) 300mW, (d) 400mW, (e) 500mW. The spin-up and down of electrons are at the throughput and drop ports, which are configured by the space-time orientation control. The polarized outputs at the throughput and drop ports, which having $(^{\pi}/_{2})$ phase difference.

Figure 4: Plot of the Hall effects sensor with the different input powers, where P1: the input power of 100mW, the sensitivity is 0.05μVT^{-1}, P2: the input power of 200mW, the sensitivity is 0.08μVT^{-1}, P3: the input power of 300mW, the sensitivity is 0.10μVT^{-1}, P4: the input power of 400mW, the sensitivity is 0.11μVT^{-1}, P5: the input power of 500mW, the sensitivity is 0.12μVT^{-1}**.**

Figure 5: The plot of the Hall mobility and electron density, with the input power, varies from 100mW-500mW, where the output is constant for all the input power.

Figure 6: The plot of the Hall effect current sensor, where P1: the input power of 100mW, the sensitivity is 0.9μVA^{-1}, P2: the input power of 200mW, the sensitivity is 0.6μVA^{-1}, P3: the input power of 300mW, the sensitivity is 0.5μVA^{-1}, P4: the input power of 400mW, the sensitivity is 0.42μVA^{-1}, P5: the input power of 500mW, the sensitivity is 0.38μVA^{-1}.

Figure 7: The plot of the response time of (a) the Hall effect current sensitivity, where P1-P5 is the input power 100-500mW, the optimum response time of 1.9fs is obtained, (b) the Hall effect sensitivity for input power 100-500mW, the optimum response time of 1.9fs is obtained.

Figure 8: The plot of the (a) the temperature Hall sensor, where P1-P5: the input power of 100-500mW, the sensitivities are 0.03μVK^{-1}, 0.015μVK^{-1}, 0.011μVK^{-1}, 0.008μVK^{-1}, and 0.006μVK^{-1} respectively, (b) Hall current sensitivity and temperature with input power of 100mW-500mW, the sensitivities of 0.9μVA^{-1}, 0.6μVA^{-1}, 0.5μVA^{-1}, 0.42μVA^{-1}, and 0.38μVA^{-1} are obtained at 100K, 200K, 300K, 400K, and 500K, respectively, (c) Hall effect sensitivity and temperature with input power of 100-500mW, the sensitivities of 0.05μVT^{-1}, 0.08μVT^{-1}, 0.10μVT^{-1}, 0.11μVT^{-1}, and 0.12μVT^{-1} are obtained at 100K, 200K, 300K, 400K, and 500K respectively, and (d) the response time of the temperature Hall sensitivities, where the optimum response time of 1.9fs is obtained.

Table 1: The selected simulation parameters (Langer et al., 1997; Prabhu, 2010)

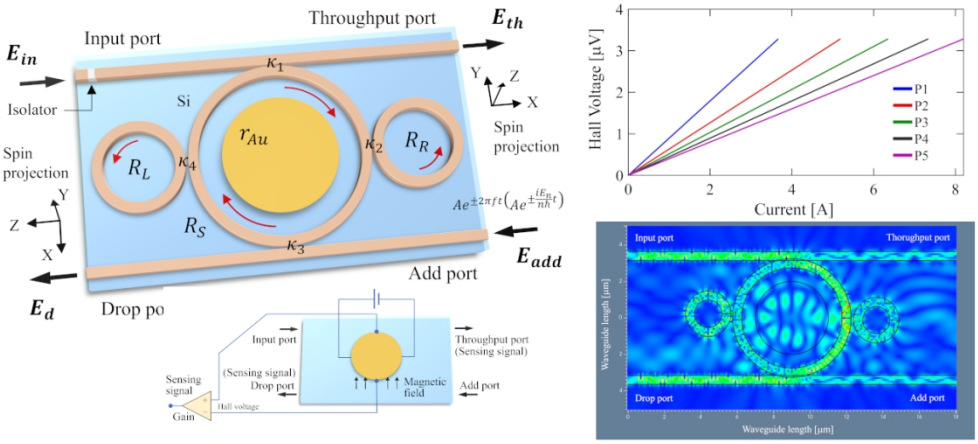
Throughput port
E_{th}
Input port
E_{in}
κ_1
Isolator
Si
r_{Au}
κ_2
R_R
Spin projection
R_L
κ_4
Spin projection
R_S
κ_3
$Ae^{\pm 2\pi f t}\left(Ae^{\pm \frac{iE_R}{n\hbar}t}\right)$
E_{add}
Add port
E_d
Drop po
Input port
Throughput port (Sensing signal)
(Sensing signal)
Drop port
Sensing signal
Magnetic field
Add port
Hall voltage
Gain
Hall Voltage [μV]
Current [A]
P1
P2
P3
P4
P5
Input port
Thoroughput port
Drop port
Add port
Waveguide length [μm]
Waveguide length [μm]

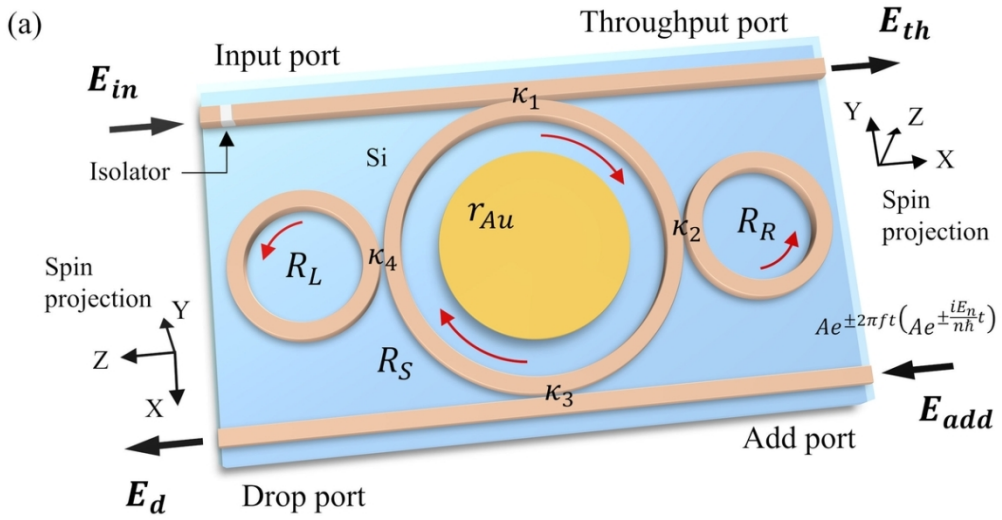

Figure 1a

101x52mm (300 x 300 DPI)

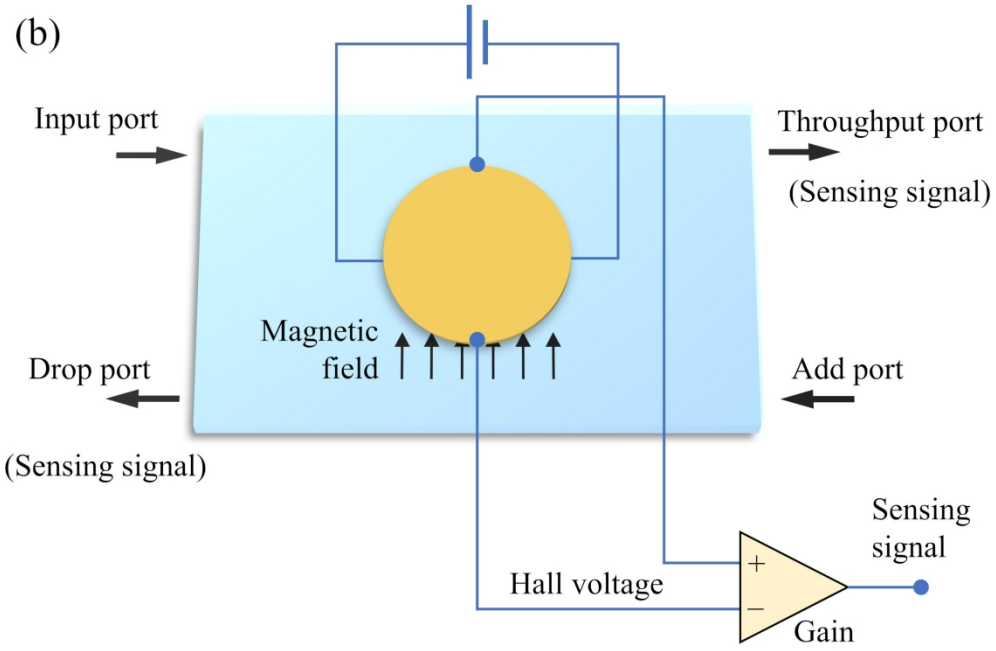
(b)
Input port
Throughput port
(Sensing signal)
Magnetic
field
Drop port
Add port
(Sensing signal)
Sensing
signal
Hall voltage
+
−
Gain

Figure 1b

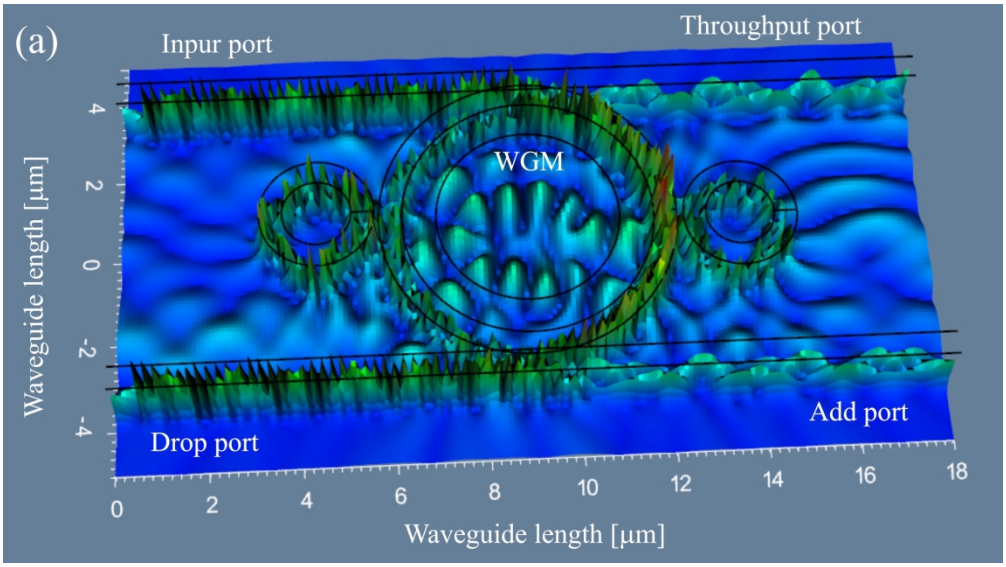
(a)
Inpur port
Throughput port
WGM
Add port
Drop port
Waveguide length [μm]
4
2
0
-2
-4
0
2
4
6
8
10
12
14
16
18
Waveguide length [μm]

Figure 2a

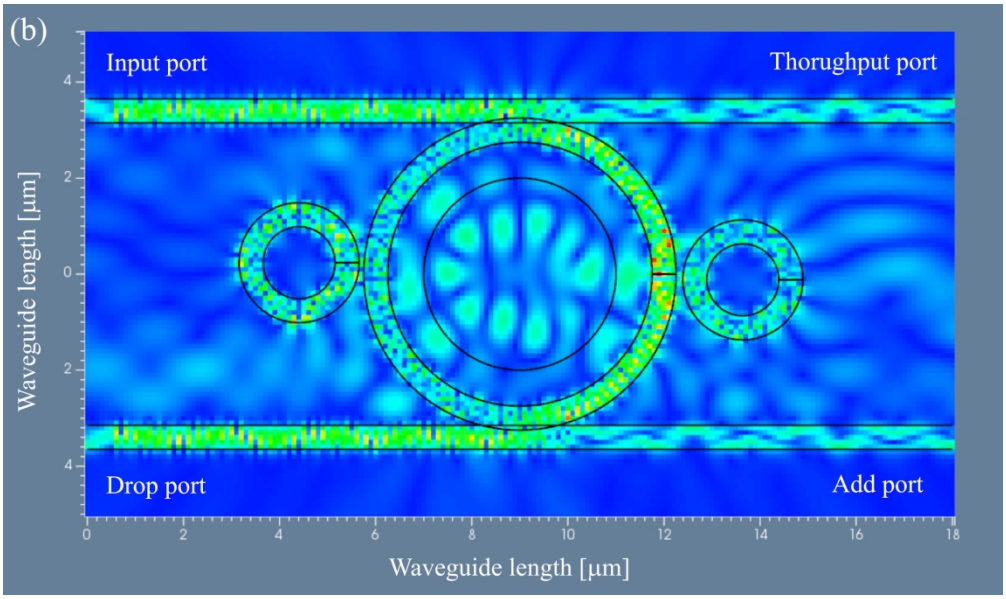
(b)
Input port
Thorughput port
Drop port
Add port
Waveguide length [µm]
Waveguide length [µm]
4
2
0
2
4
0
2
4
6
8
10
12
14
16
18

Figure 2b

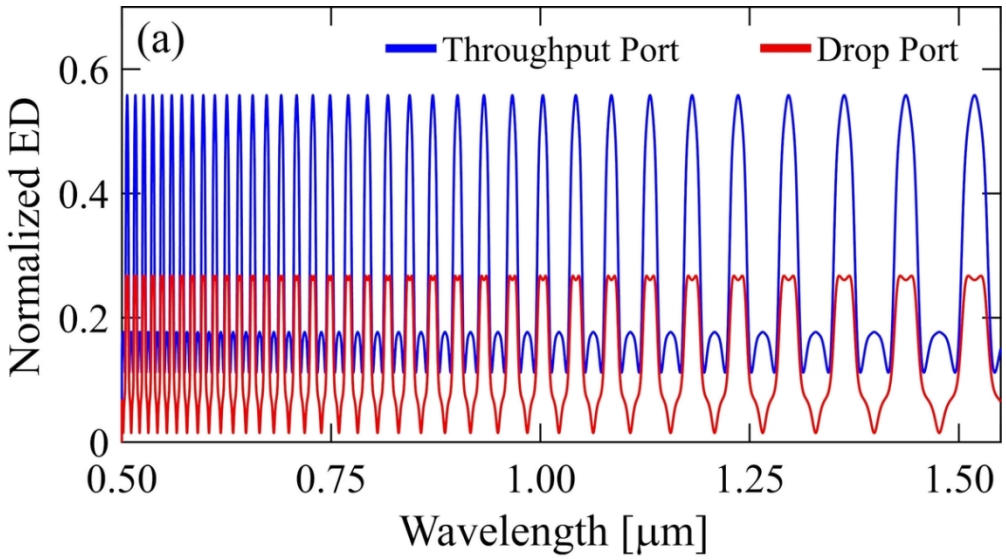

Figure 3a

101x56mm (300 x 300 DPI)

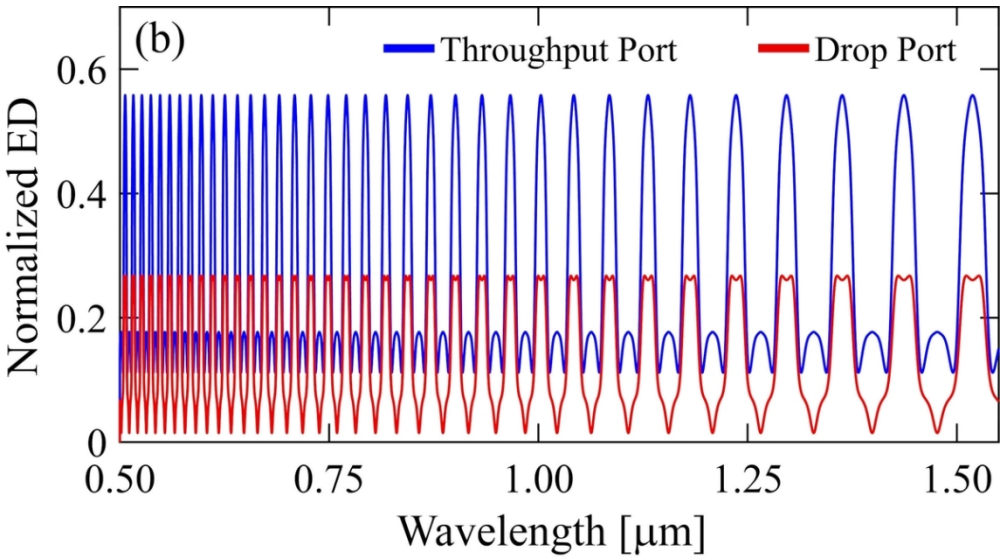

Figure 3b

101x56mm (300 x 300 DPI)

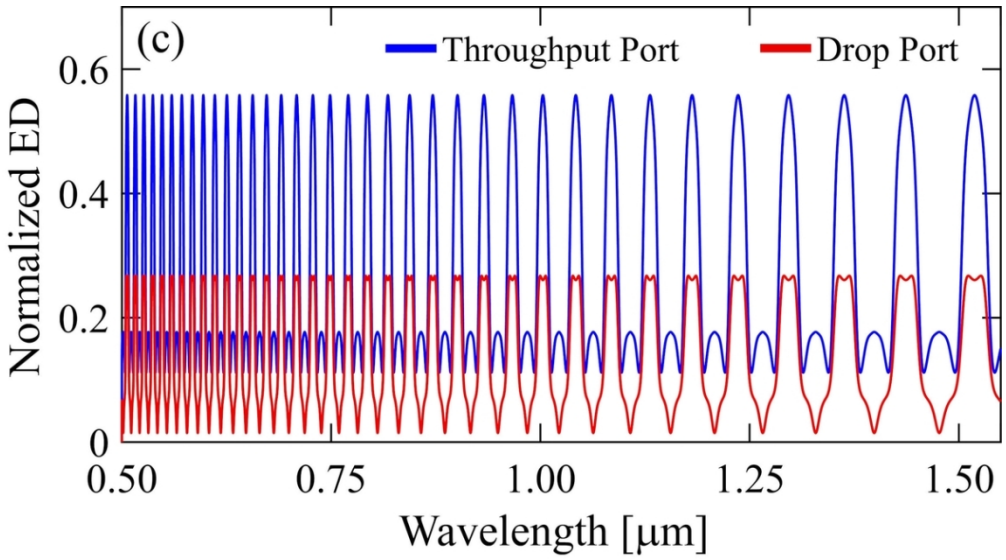

Figure 3c

101x56mm (300 x 300 DPI)

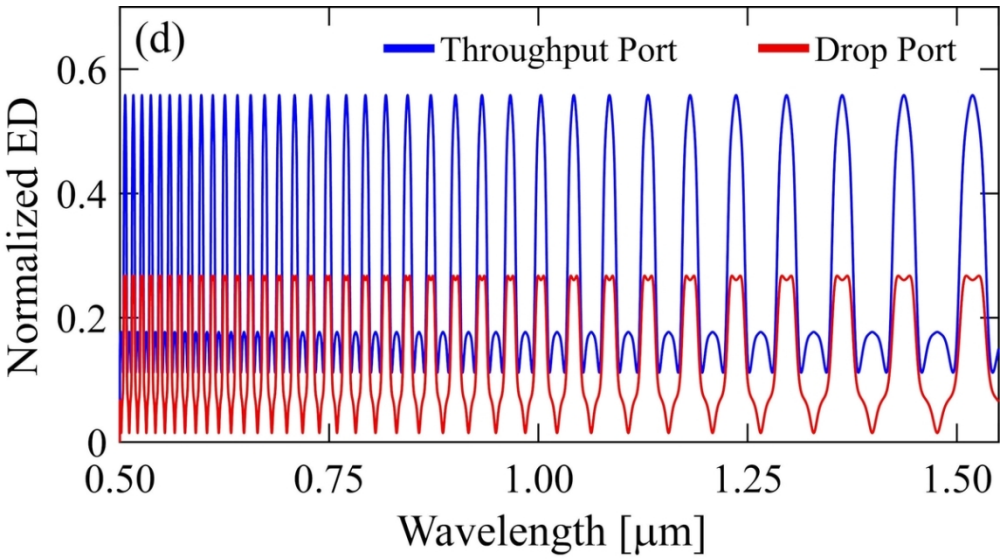

Figure 3d

101x56mm (300 x 300 DPI)

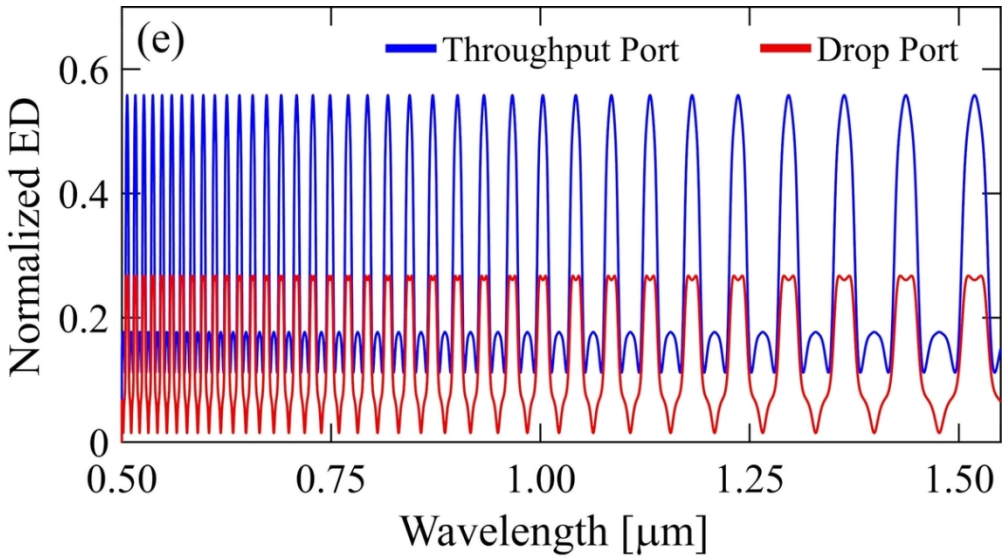

Figure 3e

101x56mm (300 x 300 DPI)

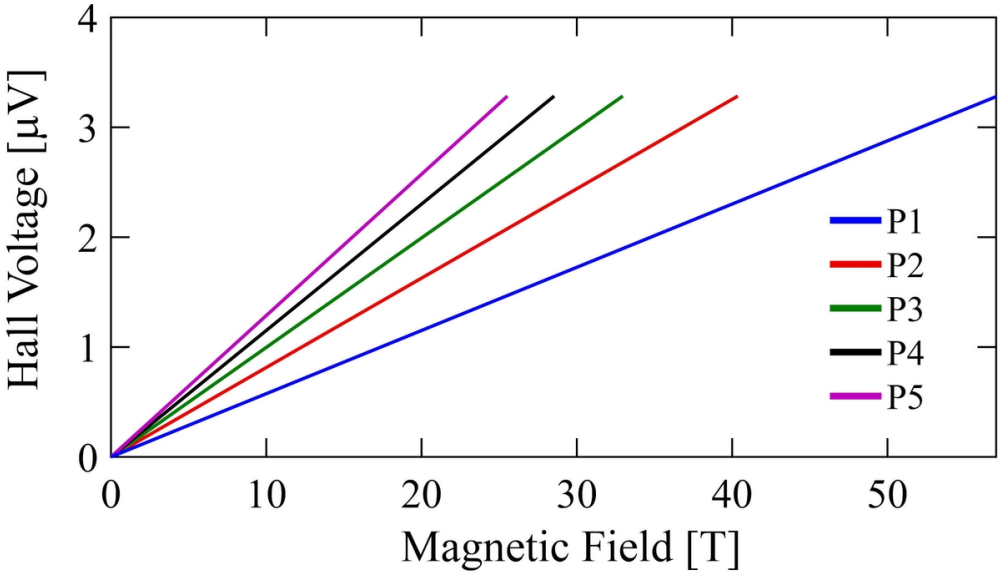

Figure 4

101x57mm (300 x 300 DPI)

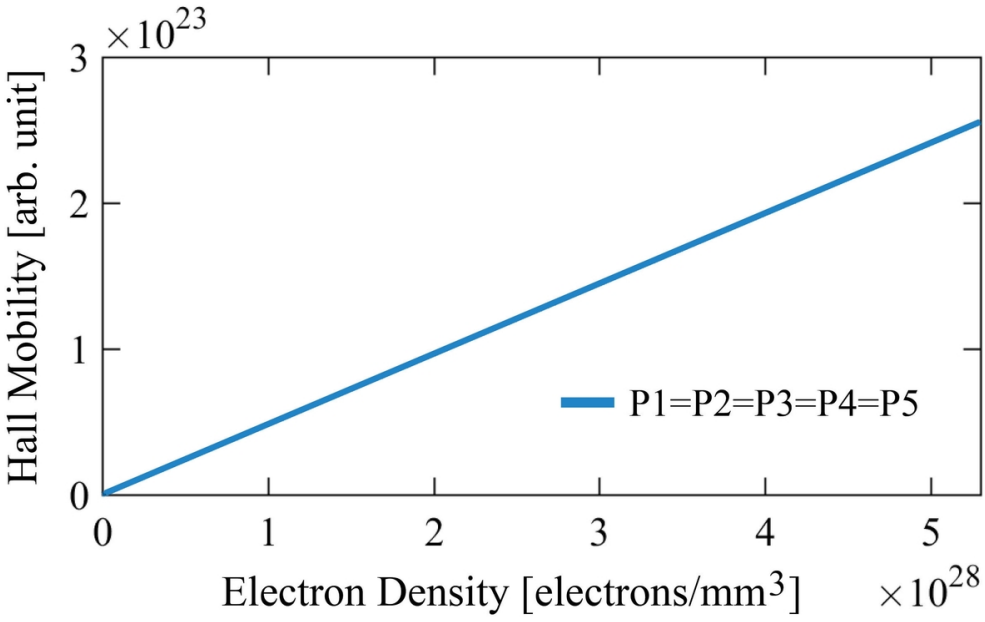

Figure 5

101x62mm (300 x 300 DPI)

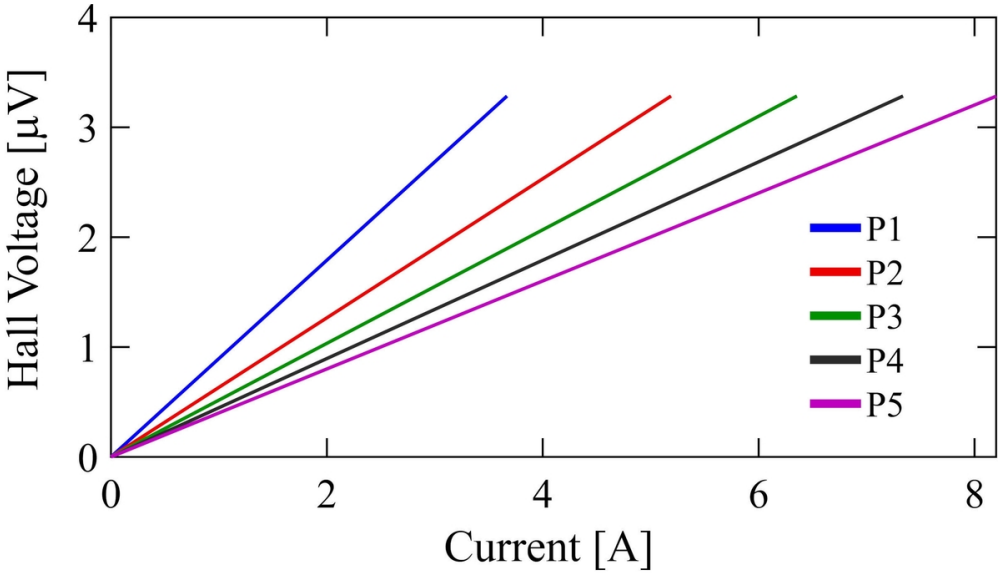

Figure 6

101x57mm (300 x 300 DPI)

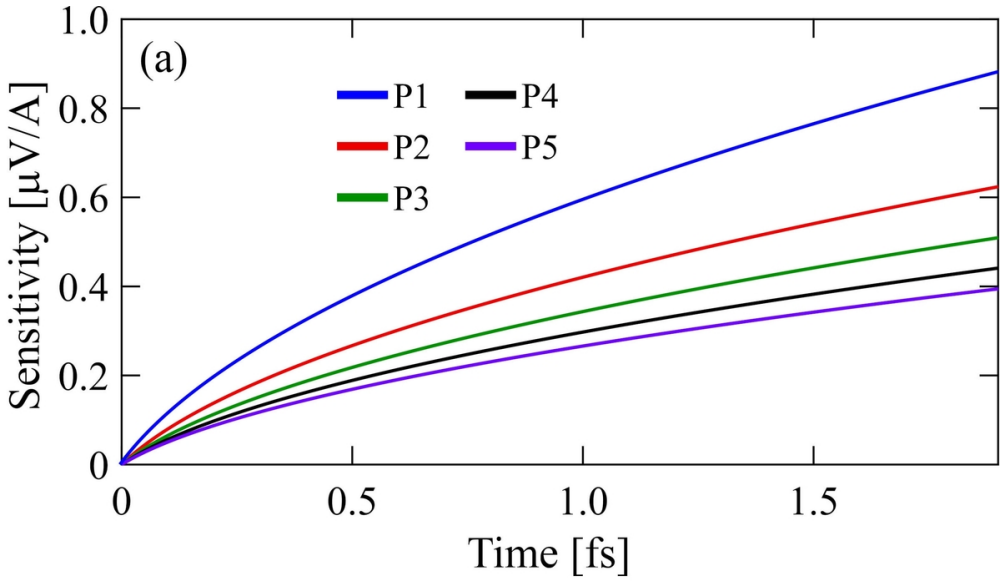

Figure 7a

101x58mm (300 x 300 DPI)

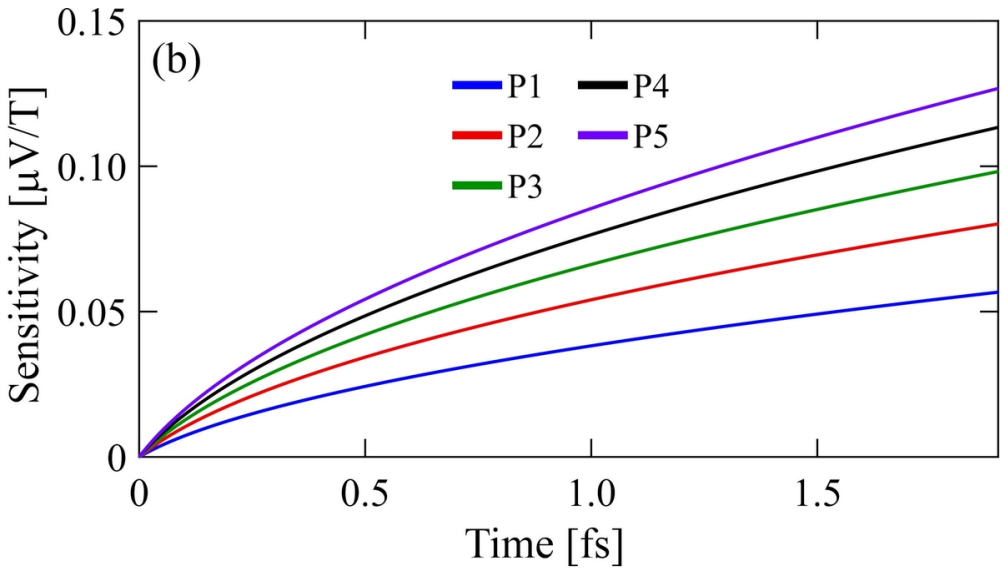

Figure 7b

101x57mm (300 x 300 DPI)

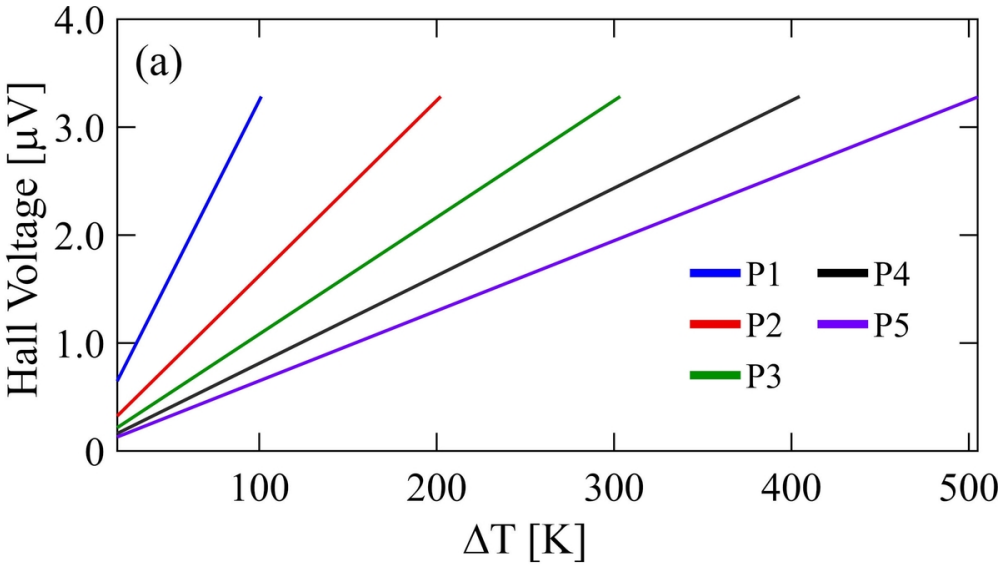

Figure 8a

101x56mm (300 x 300 DPI)

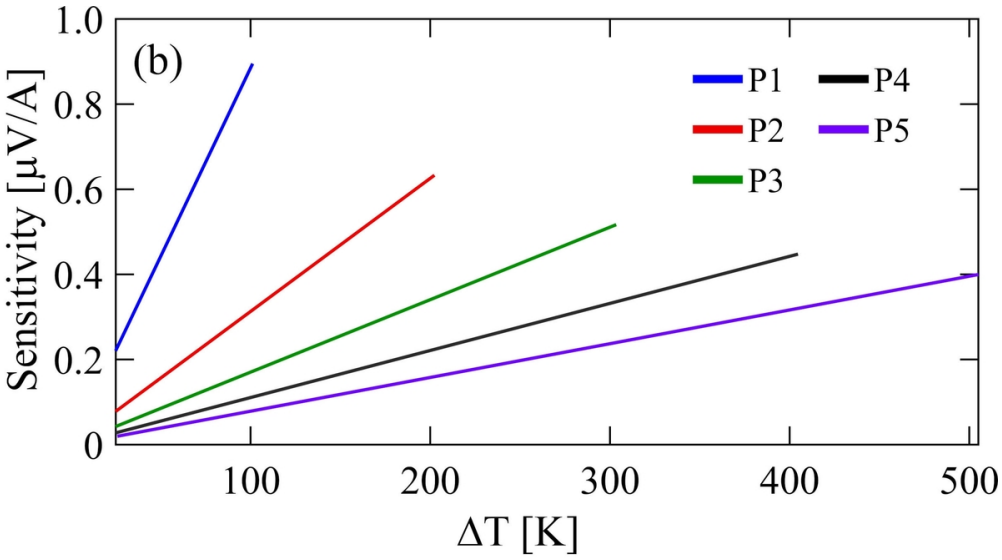

Figure 8b

101x56mm (300 x 300 DPI)

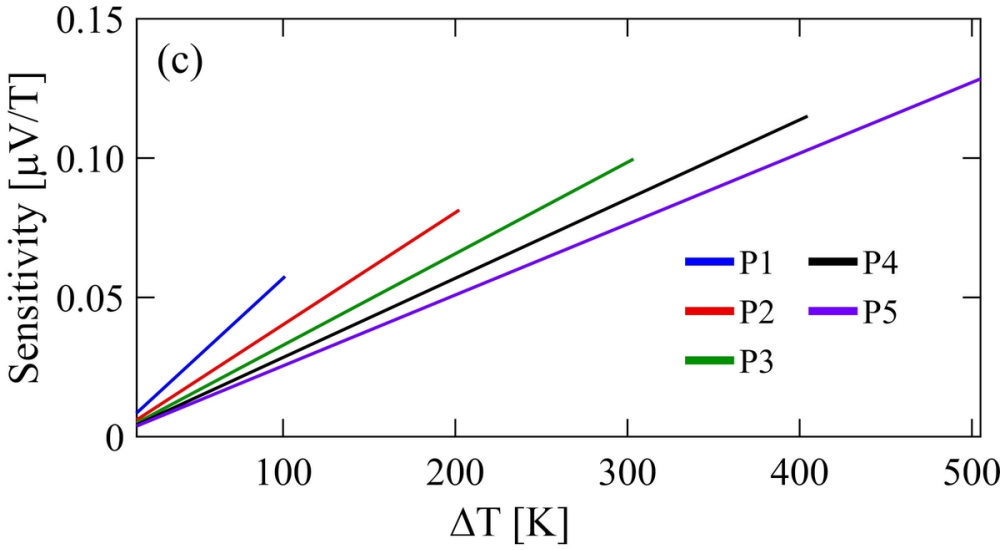

Figure 8c

101x55mm (300 x 300 DPI)

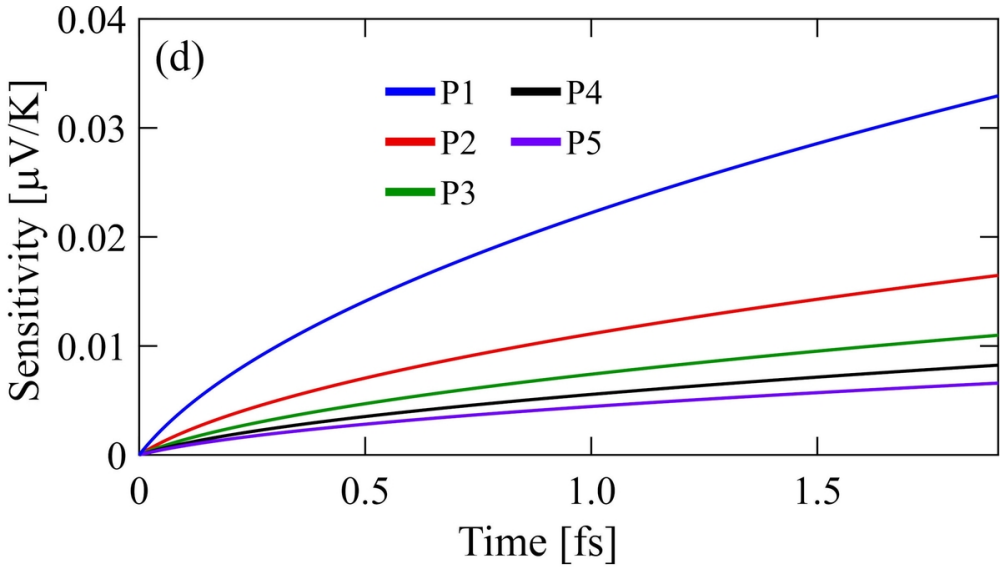

Figure 8d

101x57mm (300 x 300 DPI)

Table 1:

Parameters	Values	Units
Input light power($\boldsymbol{P_{in}}$)	100-500	mW
Gold film radius ($\boldsymbol{r_{Au}}$)	0.2-2.8	µm
Gold film thickness ($\boldsymbol{d}$)	0.1-7.5	µm
Centre ring radius ($\boldsymbol{R_s}$)	3.0	µm
Left small ring radius (R_L)	1.0	µm
Right small ring radius (R_R)	1.0	µm
Gold conductivity(σ)	4.11×10^{7}	Sm^{-1}
Gold resistivity ($\boldsymbol{\rho}$)	2.44×10^{-8}	Ωm
Au thermal conductivity ($\boldsymbol{K_{Au}}$)	310	$Wm^{-1}K^{-1}$
Coupling coefficient(κ)	0.06-0.70	
Si waveguide length ($\boldsymbol{L_{wg}}$)	16.0	µm
Si waveguide width ($\boldsymbol{W_{wg}}$)	1.5	µm
Insertion loss ($\boldsymbol{\gamma}$)	0.50	dB
Au refractive index ($\boldsymbol{n_{Au}}$)	1.80	
Si refractive index ($\boldsymbol{n_{Si}}$)	3.42	
Si nonlinear refractive index ($\boldsymbol{n_2}$)	$1.3\text{x}10^{-13}$	m^2W^{-1}
Input light wavelength(λ)	1.55	µm
Plasma frequency ($\boldsymbol{\omega_p}$)	$1.299\text{x}10^{16}$	$rads^{-1}$
Core effective area ($\boldsymbol{A_{eff}}$)	0.30	μm^2
Free space permittivity ($\boldsymbol{\epsilon_o}$)	$8.85\text{x}10^{-12}$	Fm^{-1}
Electron mass ($\boldsymbol{m}$)	$9.11\text{x}10^{-31}$	kg
Electron charge ($\boldsymbol{q}$)	$1.60\text{x}10^{-19}$	Coulomb
Waveguide loss($\boldsymbol{\alpha}$)	0.50	$dB.(mm)^{-1}$